Microchimica Acta (2025) 192:662
https://doi.org/10.1007/s00604-025-07502-5

RESEARCH

# Carbon nanofiber–enhanced molecular imprinted electrochemical sensor for hypoxanthine detection

Canan Armutcu[1] · Sena Pişkin[1] · Erdoğan Özgür[1] · Mustafa Karakaya[3] · M. Emin Çorman[2] · Lokman Uzun[1]

Received: 14 May 2025 / Accepted: 16 August 2025 / Published online: 12 September 2025


## Abstract

A molecularly imprinted electrochemical sensor (MIP) was developed using thymine-functionalized carbon nanofibers (Thy@CNFs) to enable selective detection of hypoxanthine (HYP). The sensor was fabricated by first depositing Thy@CNFs onto a glassy carbon electrode (GCE), followed by electropolymerization of a pyrrole-co-pyrrole-3-carboxylic acid (Py-co-PyCOOH) copolymer in the presence of HYP. Each modification step was characterized using electrochemical impedance spectroscopy (EIS), cyclic voltammetry (CV), attenuated total reflection-Fourier transform infrared spectroscopy (ATR-FTIR), scanning electron microscopy (SEM), and contact angle measurements. Under optimized conditions, the Thy@CNFs-modified MIP sensor (Thy@CNFs/MIP/GCE) exhibited a linear response to HYP concentrations ranging from $1\times10^{-9}$ to $1\times10^{-8}$ M, with a detection limit of $1.71\times10^{-10}$ M. Finally, the sensor was successfully applied to commercial serum and artificial urine sample, achieving recoveries of 99.55% and 100.17%, respectively, demonstrating its accuracy, precision, and practical applicability in real sample analysis.

**Keywords** Hypoxanthine · CNFs · Thymine · Molecular imprinting · Modified glassy carbon electrode · Differential pulse voltammetry

## Introduction

Hypoxanthine (HYP) is a biologically significant purine derivative that plays a critical role in various metabolic and pathological processes. Hypoxanthine, a purine derivative, is a major catabolite of ATP that accumulates under conditions of cellular stress, particularly during ischemia and hypoxia, making it a valuable biomarker for monitoring tissue damage [1]. Elevated hypoxanthine levels have been detected in clinical conditions such as schemia and sepsis, where it reflects oxidative stress and impaired oxygen delivery [2]. Hypoxanthine also plays a role in gout and disorder of purine metabolism disorders, Lesch-Nyhan syndrome, where HGPRT deficiency and excessive accumulation lead to elevated uric acid levels [3]. Several well-established analytical methods have been used for detecting hypoxanthine, such as high-performance liquid chromatography (HPLC), mass spectrometry (MS), and spectrophotometric method. Although these techniques provide selectivity and low detection limits, they rely on high costs, labor, and extended analysis times [4]. Given its broad relevance across clinical domains and its potential for rapid, sensitive detection, hypoxanthine serves as a promising target for biosensor development in both diagnostic and monitoring applications.

In recent years, molecularly imprinted electrochemical sensors (MIECs) have emerged as a more efficient and cost-effective alternative, offering superior sensitivity, selectivity, and rapid response [5–7]. Electrochemical techniques, along with their advantages such as sensitivity, ease of use, and low cost, have played a leading role in modern bioanalytical sensing and have provided a variety of possibilities for biomolecular detection. Inspired from nature's perfect harmony, the integration of novel recognition algorithms has pave the way for increasing the potential of biosensors with diverse innovations finding their roots in the field of organic bioelectronics [8]. These sensors incorporate molecularly imprinted polymers (MIPs) that create specific recognition

✉ Canan Armutcu
cananarmutcu@hacettepe.edu.tr

[1] Faculty of Science, Department of Chemistry, Hacettepe University, Ankara, Turkey

[2] Gülhane Faculty of Pharmacy, Department of Biochemistry, University of Health Sciences, Ankara, Turkey

[3] Faculty of Engineering & Architecture, Department of Energy Systems, Sinop University, Sinop, Turkey

sites tailored to template molecules, thereby facilitating precise detection even within complex biological or food matrices. Given these advantages, MIECs are increasingly recognized as a promising platform for real-time, on-site monitoring in clinical diagnostics [9].

Furthermore, carbon-based nanostructures have attracted the researchers' attention to develop efficient biosensors for detecting biomolecules at the lowest detection limit and make them potentially applicable [10]. Carbon-based nanostructures have become one of the most widely used composite materials in sensor designs owing to their superior advantages such as the shape, excellent conductivity, high porosity, and high surface area of the composite material [11].

In this context, carbon nanofibers (CNFs), one of the intriguing carbon-based nanomaterials, are unbound three-dimensional nanostructures and are often used as nanomaterials to modify surfaces for enhanced features. CNFs are inclined to interacting with molecules and particles, thanks to their excellent electrical conductivity and high surface area, which make them ideal modifying agents to develop influential electrode materials [12]. In addition, their catalytic capabilities increase their uses in sensor studies and make them the one of hot topics in the literature [13].

Conducting polymers (CPs) are also one of the key polymers for developing organic bioelectronic interfaces. They are being intensively investigated due to their good conductivity, easy to prepare, low production costs, and good stability in different environments. These polymers have been used in a many applications, including electronic devices, energy storage systems, (bio)sensors, solar cells, and unique physicochemical applications [14]. CPs effectively close the gap between living systems and modern electronics by providing a flexible and adaptable interface that changes its electronic conductivity depending on the ionic contribution of the biological environment [15]. Moreover, high biocompatibility, the low impedance, and wide range of applications of CPs make them promising candidates to transform the detection of biomolecules. The use of CPs as active materials in both electrodes and transistors has enwidened opportunities for biosensing using antibodies, enzymes, and aptamers [16]. In recent years, research on CPs has attracted increasing interest while the numbers of studies using CPs including polydopamine (PDA), polyaniline (PANI), polyacetylene (PA), poly(para-phenylene) (PPP), poly(3,4-ethylenedioxythiophene):polystyrene sulfonate (PEDOT:PSS), polypyrrole (PPy), poly(phenylenevinylene) (PPV), and polythiophene (PTH) have been exponentially increased [17]. Among them, PPy, also being used as a component of carbon nanostructured composite materials, is a unique conducting polymer due to its good redox properties, electrical conductivity, and good thermal stability [18].

Herein, we focused our efforts to develop an efficient electrochemical sensor for detecting hypoxanthine from commercial serum and artificial urine sample via combining excellent features of molecular imprinting, conducting polymers, and carbon nanofibers into a unique study. The rationale for using thymine as a specific ligand in this study is its molecular compatibility with hypoxanthine (HYP). Computational modeling studies were performed to evaluate the possible interactions between HYP and thymine or uracil. Among those tested, thymine showed the most favorable binding affinity compared to uracil, indicating a higher potential for selective interaction. In addition, thymine contains a primary amine group that facilitates covalent immobilization onto oxidized carbon nanofibers (CNFs) via amide bond formation.

Thus, this study established thymine as an optimum recognition element for molecular imprinting process targeting HYP in terms of high theoretical affinity and chemical reactivity. The study demonstrates the combined use of molecular imprinting and conducting polymers to enhance molecular recognition capabilities. This was achieved by electropolymerizing pyrrole-based monomers around hypoxanthine (HYP) molecules on thymine-modified carbon nanofibers (Thy@CNFs) integrated into glassy carbon electrodes (Thy@CNFs/MIP/GCE). Pyrrole is a well-known conducting monomer extensively utilized in electrochemical sensors, and it can form stable, long polymeric chains. However, it lacks specific functional groups that can establish strong interactions with template molecules, which may limit imprinting efficiency and binding specificity. In contrast, pyrrole-3-carboxylic acid contains functional groups that facilitate specific interactions, such as hydrogen bonding with the template molecule, hypoxanthine (HYP). These interactions enhance the formation of well-defined recognition sites. Therefore, pyrrole was employed to provide structural integrity and conductivity to the polymer matrix, while pyrrole-3-carboxylic acid was co-polymerized [19, 20] to introduce the functional sites necessary for the selective binding of HYP. Each modification step and materials developed was comprehensively characterized by electrochemical impedance spectroscopy (EIS), cyclic voltammetry (CV), attenuated total reflection-Fourier transform infrared spectrophotometry (ATR-FTIR), scanning electron microscopy (SEM), and contact angle measurements. After that, sensor performances and selectivity studies were performed via differential pulse voltammetry after optimizing the affecting parameters.

## Experimental

### Instrumentation

Electrochemical measurements were accomplished on a PalmSens4 potentiostat/impedance analyzer (Palmsens BV, Netherland) and controlled by PSTrace software. A glassy carbon electrode (GCE, diameter: 3.0 mm) serves as the working electrode. A conductive Ag/AgCl electrode was employed as a reference electrode whereas a platinum wire was utilized as a counter electrode. Chemical composition of the working electrode was analyzed using ATR-FTIR spectroscopy in the range of 4000–650 $cm^{-1}$ at 2 $cm^{-1}$ resolution, model ATR-FTIR 8000 series (Shimadzu, Tokyo, Japan). The surface morphology of the working electrode was visualized using a scanning electron microscope (TESCAN GAIA 3, Czech Republic) with an acceleration voltage of 10 kV and magnification of 500×.

### Reagents and solutions

Graphitized carbon nanofibers (200–600 nm in diameter, 5–50 mm in length) were supplied by Grafen Chemical Industries Co. (Ankara, Turkiye). Hypoxanthine, xanthine, thymine, uracil, pyrrole, and pyrrole-3-carboxylic acid were purchased from Merck (Darmstadt, Germany). Additional reagents included potassium ferricyanide ($K_3[Fe(CN)_6]$; ≥ 98.5%) and potassium ferrocyanide ($K_4[Fe(CN)_6]0.3H_2O$; ≥ 99.0%), potassium chloride (purity: ≥ 99), and methanol (purity: > 99%) were all obtained from Sigma-Aldrich (Darmstadt, Germany). All other chemicals and reagents were of analytical grade and prepared by deionized water (DI, 18 MΩ.cm) obtained from a Puris ultrapure water system.

### Computational design

In the first stage of the study, uracil and thymine were evaluated to identify which would interact most effectively with the target molecule (HYP). The most suitable ligand for HYP was then determined using theoretical calculations. For this aim, the optimizations of interaction simulations, energy calculations, and hydrogen bond parameters were carried out in Density Functional Theory (DFT), B3LYP hybrid functional approach, and 6–31 + + G(*d,p*) basis set as a computational quantum mechanical modeling method [21, 22]. The interaction energies were concluded in counterpoise approach [23]. This approach is a method that calculates corrected/uncorrected complexation energy and basis set superposition error (BSSE) energy for interactions. Natural atomic orbital and bond orbital analyses were carried out in Gaussian NBO Version 3.1 [24] meanwhile input files and modeling of the optimized structures were viewed in Gauss View program [25]. Donor and acceptor regions in hydrogen bond interaction between the target molecule and the functional ligands were interpreted through the Discovery Studio Visualizer v21 program at the final of Gaussian computations [26]. All the calculations on optimizations of the interactions were completed with the help of Gaussian 09 W software package.

### Thymine immobilization onto CNFs (Thy@CNFs)

Based on theoretical calculations, thymine (Thy) was selected as a ligand to enhance the selectivity of the electrochemical sensors developed for the detection of hypoxanthine (HYP). To achieve this, carbon nanofibers (CNFs) were first treated with nitric acid to introduce carboxylic acid (-COOH) functional groups onto their surface, enabling subsequent covalent immobilization of thymine (Thy) molecules via a substitution reaction.

The oxidized CNFs were then reacted with thionyl chloride ($SOCl_2$) to convert the carboxylic groups into more reactive acyl chlorides (-COCl), which serve as effective leaving groups. Thymine, containing primary amine functionalities, was subsequently introduced into the reaction medium, facilitating the formation of amide bonds and yielding thymine-functionalized CNFs (Thy@CNFs). Scheme 1 illustrates (a) the chemical pathway for thymine immobilization on CNFs and (b) the proposed interaction mechanism between Thy@CNFs and the target molecule, hypoxanthine (HYP).

### The synthesis of Thy@CNF-assisted molecularly imprinted electrochemical sensor (MECs)

Herein, a glassy carbon electrode (GCE) was used as a working electrode and as a substrate during molecular imprinting approach. In this context, GCE is first washed with the methanol and DI solution (50:50, v/v) for 3 min and then polished with alumina on a polishing cloth to remove any impurities on the electrode surface. After rinsing it with DI, it was dried and kept in dust-free environment before use. Afterward, the dispersion of Thy@CNFs (1.0 µL) employed not only to improve the conductivity of the electrode but also to orientate the HYP molecules at the interface of CNF and MIPs was drop-casted on the polished GCE surface. At the polymerization step, molecularly imprinted polymeric film was synthesized by electropolymerization with Py (0.05 M), PyCOOH (0.01 M),

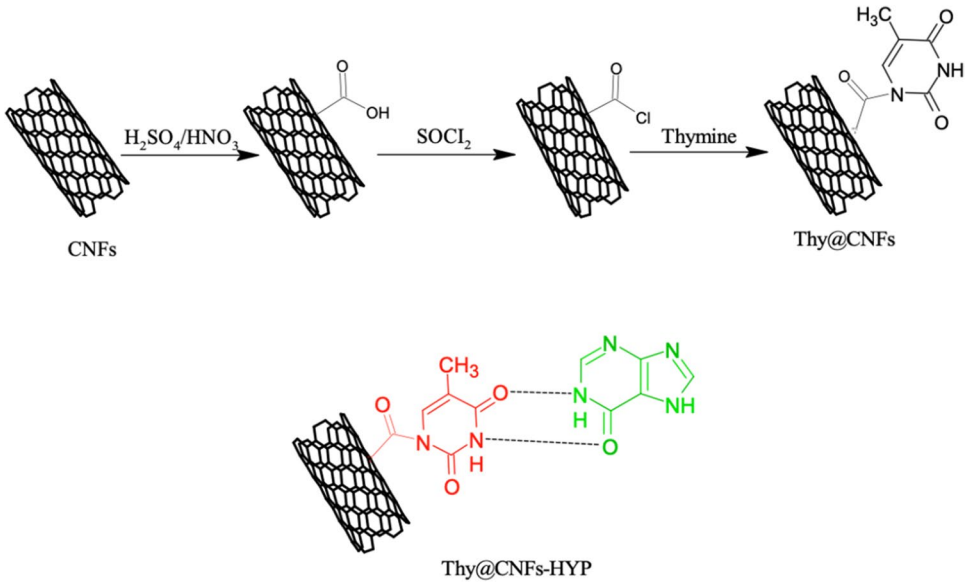


**Scheme 1** Schematical representation of Thy immobilization onto CNFs and proposed interaction mechanism of CNFs@Thy and HYP

and HYP (0.01 mM) (the template molecule) in PBS (pH 7.4, 10 mM) solution bearing $LiClO_4$ (0.1 M) by applying CV in the potential range between − 0.2 and 1.2 V at 100 mV/s. After polymerization, HYP was removed to leave behind a complementary cavity within a polymeric network. For comparison purpose, the non-imprinted polymeric film (NIP) was also synthesized via same procedure employed for the MIP without including the template molecule. Electrochemical measurements were performed using cyclic voltammetry (CV), and differential pulse voltammetry (DPV) with a redox couple $[Fe(CN)_6]^{3-/4-}$.

## Real samples

The sensor's performance and applicability for clinical diagnostics were assessed using commercial serum and artificial urine sample as real sources of the HYP. For the preparation of spiked commercial serum samples, a precise volumetric combination was employed: 1.0 mL of a 10 mM HYP solution was mixed with 3.6 mL of commercial serum sample and 5.4 mL of acetonitrile in a test tube. This combination resulted in a total volume of 10.0 mL and a final concentration of 1.0 mM for the HYP in the prepared serum solution. The mixture was then sonicated for 15 min, followed by centrifugation at 5000 rpm for 20 min to precipitate protein residues. Similar preparation procedure was followed for the urine sample. According to a commonly used protocol [27], artificial urine spiked with HYP at a final concentration of 1.0 mM was used. Recovery studies were conducted based on data obtained from the calibration equation. Recovery values were determined by spiking aliquots of the prepared commercial serum and urine sample with known concentrations of the HYP solution. For each investigated concentration level, the percentage relative standard deviation (%RSD) values were calculated. Recovery tests were also performed to evaluate the accuracy of the fabricated sensor by using the high-performance liquid chromatography (HPLC) standard method. The HPLC method is described in detail in the Supplementary File.

# Results and discussion

## Quantum calculations for designing of MECs

The orientation and interaction tendency of target molecules is one of the key parameters to design MECs with efficient selectivity and proper specificity.

In this respect, comparative theoretical calculations were performed to choose the proper functional ligand to orientate target molecule, HYP at the electrode interface. Herein, two pyrimidine derivatives, Thy and uracil (Ura), were chosen as potential molecules due to their structures, which are complementary to HYP (one of purine derivatives) The types of interaction between HYP and Thy/Ura were tested to identify the most effective structure by using a computational method. The possible forms of HYP-Ura and HYP-Thy interactions are visualized via the Discovery Studio Visualizer v21. The relative energies of other possible interaction forms in the structures are summarized in Fig. 1. In both HYP-Thy interactions, *form1* structures have lower total energies and interaction energies. *N1*−H1···*O2* and *N2*−H2···*O1* conventional type of H-bonds in HYP-Thy structures attract attention. Donor and acceptor

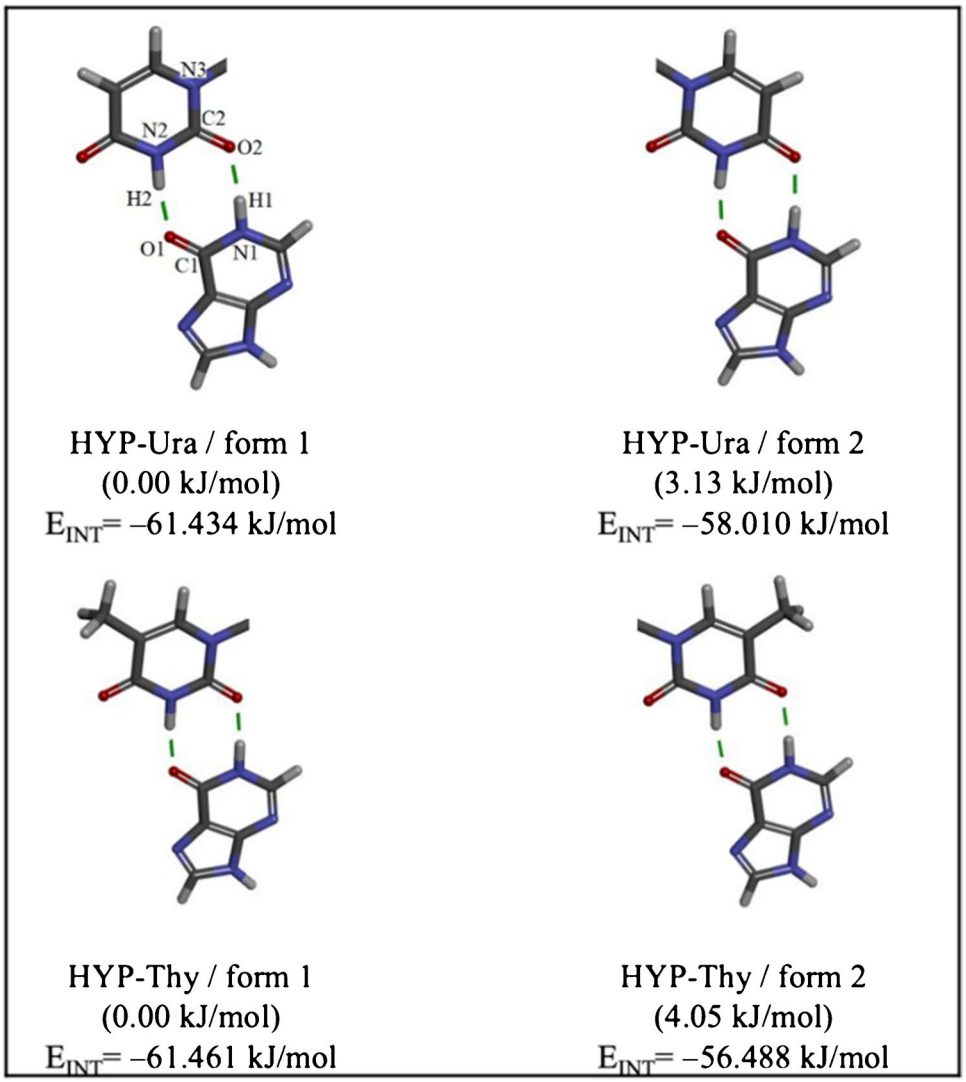


**Fig. 1** The optimized models of HYP-Thy/Ura interactions with relative energies of the interaction forms (given in parentheses)

groups on the hydrogen bonds of the HYP-Thy structures are N−H and C = O structures, respectively.

In the study, stabilization energies of bonding-antibonding interactions for the H-bond regions in NBO basis have also been calculated by electronic structural methods. Here, with the help of 2nd order perturbation theory, stabilization energies and all possible donor–acceptor interactions between filled Lewis type NBOs and empty non-Lewis type NBOs can be interpreted. In this concept, $n_{(O1)} \rightarrow \sigma_{(N2\text{-}H2)}^*$ interaction between the oxygen lone pair and *N2*-H2 antibonding shows strong stabilization with values of 53.717 kJ/mol in HYP-Ura (*form 1*) structure, *N2*−H2···*O1* conventional type H-bond. The stabilization energy value for $n_{(O2)} \rightarrow \sigma_{(N1\text{-}H1)}^*$ interaction in HYP-Ura (*form 1*) structure is 43.543 kJ/mol.

On the other hand, the stabilization energy values for $n_{(O1)} \rightarrow \sigma_{(N2\text{-}H2)}^*$ and $n_{(O2)} \rightarrow \sigma_{(N1\text{-}H1)}^*$ interactions in HYP-Thy (*form 1*) structure are 50.744 and 46.934 kJ/mol, respectively.

**Table 1** Total energy and interaction energy values

| Structures | Total energy (a.u) | Interaction energy $E_{INT}$ (kJ/mol) | H1···*O2* Distance (Å) | H2···*O1* Distance (Å) |
|---|---|---|---|---|
| HYP-Ura | −901.418 | −61.434 | 1.835 | 1.790 |
| HYP-Thy | −940.747 | −61.461 | 1.820 | 1.807 |

According to these results, the stabilizations on the *N2*−H2···*O1* interactions are stronger in both HYP-Thy/Ura structures.

Table 1 summarizes the corrected interaction energies ($E_{INT}$), total energies, and H-bond parameters. Herein, it was aimed to interpret the strong interaction between HYP and the ligands. According to H-bond geometry results, the binding ability in *N2*−H2···*O1* is stronger than the other hydrogen bonds for both HYP-Thy structures. The interaction energy (corrected) values indicate that HYP-Thy interaction

is more effective than HYP-Ura interaction. In this respect, Thy was chosen as an orienting ligand for HYP imprinting procedure. Thymine contains a methyl group (–$CH_3$) at the 5-position of its pyrimidine ring, which may enhance the electron density around its carbonyl oxygen and nitrogen atoms. This increased electron density facilitates the formation of hydrogen bonds with hypoxanthine, making thymine more effective in this regard. Additionally, the presence of the methyl group may influence the spatial arrangement of thymine, allowing for better alignment with hypoxanthine. This optimal orientation can lead to stronger hydrogen bonding interactions between the two molecules.

Furthermore, energy gaps between the highest occupied molecular orbital ($E_H$) and the lowest unoccupied molecular orbital ($E_L$) and visuals have been obtained by B3LYP approach (Fig. S1).

In molecular structures, $E_H$ and $E_L$ energy values represent the ability to donate and accept electrons, respectively, whereas the energy gap ($E_H$–$E_L$) gives results about molecular chemical stability [28]. In the frontier molecular orbitals (FMOs) visuals, the red and green regions represent positive and negative diffuse ambient lights, respectively. For the HYP-Ura and HYP-Thy structures, the FMO distributions at the $E_H$ level is clearly concentrated on HYP, and the $E_L$ distributions are concentrated on Ura and Thy, respectively. $E_H$ value of the HYP increased while the $E_L$ value decreased in both interactions.

In addition, $E_H$ and $E_L$ values increase when Ura and Thy structures interact with HYP as expected. In both cases, the energy gaps have been computed at the values lower than those of Ura, Thy, and HYP, which pointed out the electron density variation with respect to the selective interaction.

Moreover, the interactions of the HYP with Ura and Thy were considered by applying the visuals mapped with electrostatic potential (ESP) (Fig. S2). Negative and positive ESP are used to explore the electron richness or poorness of the molecular regions and to discuss the suitability of the electrophilic and nucleophilic attack. The negative ESP generally refers to the lone pair of an electronegative atom [29]. Electrostatic potential, V($r$), is defined in terms of interaction energy between electrical charge generated from electrons and nuclei of molecules and a positive charge located at any given point $r$(x,y,z) around a molecule [30, 31]. Red, green, and blue tones represent negative, neutral, and positive potential distribution, respectively. Minimum V($r$) are calculated for HYP-Ura and HYP-Thy interactions as approximately – 29.85 and – 44.95 kJ/mol, respectively, around the oxygen (O1) atoms in *N2*–H2···*O1* conventional type H-bonds. In the light of potential distribution and V($r$) values, it was determined that Thy molecules created a complex with the target molecules, HYP that is stronger than Ura did.

## Characterization of materials

According to the theoretical data observed, molecularly imprinted electrochemical sensors were developed on GCE surface while comprehensive characterization studies were performed at each modification step. Firstly, the surface characteristics of materials were examined using the ATR-FTIR measurements (Fig. 2A). The bands observed in the spectra around 3300 $cm^{-1}$ and 3100 $cm^{-1}$ belong to the -OH stretching and NH bending, originating from PyCOOH and Thy, respectively. The ring stretching bands (C-N, C = N, C–C, and C = C groups) stemmed from both Thy and Py structures have been obtained at 1567 $cm^{-1}$, 1486 $cm^{-1}$, 1314 $cm^{-1}$, and 1045 $cm^{-1}$, respectively. The peaks at 1700 $cm^{-1}$ may be contributed to the C = O stretching bands whereas other band at 796 $cm^{-1}$ may be owing to C–N deformation corresponding to Thy as well. These results confirm that polymeric material was successfully synthesized on GCE surface.

In the ATR-FTIR spectra of imprinted and non-imprinted polymeric films, no significant differences were observed because of the use of the same monomers which resulted in similar polymeric backbones. The morphologies of polymeric films on GCE surfaces were observed by SEM analyses, providing detailed information about their morphological features (Fig. 2B).

Figure 2B1 shows SEM images of bare Thy@CNFs were randomly distributed on the surface of GCE meanwhile the particle-like structures were formed with average surface roughness for NIP and MIP (Fig. 2B2/3). Additionally, the surface roughness of the Thy@CNFs/MIP/GCE sensor surface (MIP) was slightly higher than that of NIP version. In addition, to confirm the variations in surface roughness and water compatibilities of MIP and NIP sensors, contact angle measurements were also performed (Fig. 2C). The contact angle of the bare GCE (**C1**) decreased after modifying with Thy@CNFs from 128.6 to 95.5° (Fig. 2C1/C2). The results supported the random distribution of Thy-modified CNFs on GCE surface, which increased roughness and water compatibility of the GCE electrode as well as being consistent with SEM observations.

Furthermore, the contact angle values for MIP (Fig. 2C3) and NIP (Fig. 2C4) were determined as 60.8° and 72.5° respectively, which clearly indicated the hydrophilic surface with rough topography was formed by modification and polymerization steps, while a slight variation between MIP and NIP surfaces was directly related to roughness changes due to polymerization regime which was differed in the presence of template molecules in the environment. Besides, MIP has more hydrophilic characters depending on the formation of imprinted cavities through the polymeric film. In both cases, the bearing of hydroxyl-, carboxyl-, and

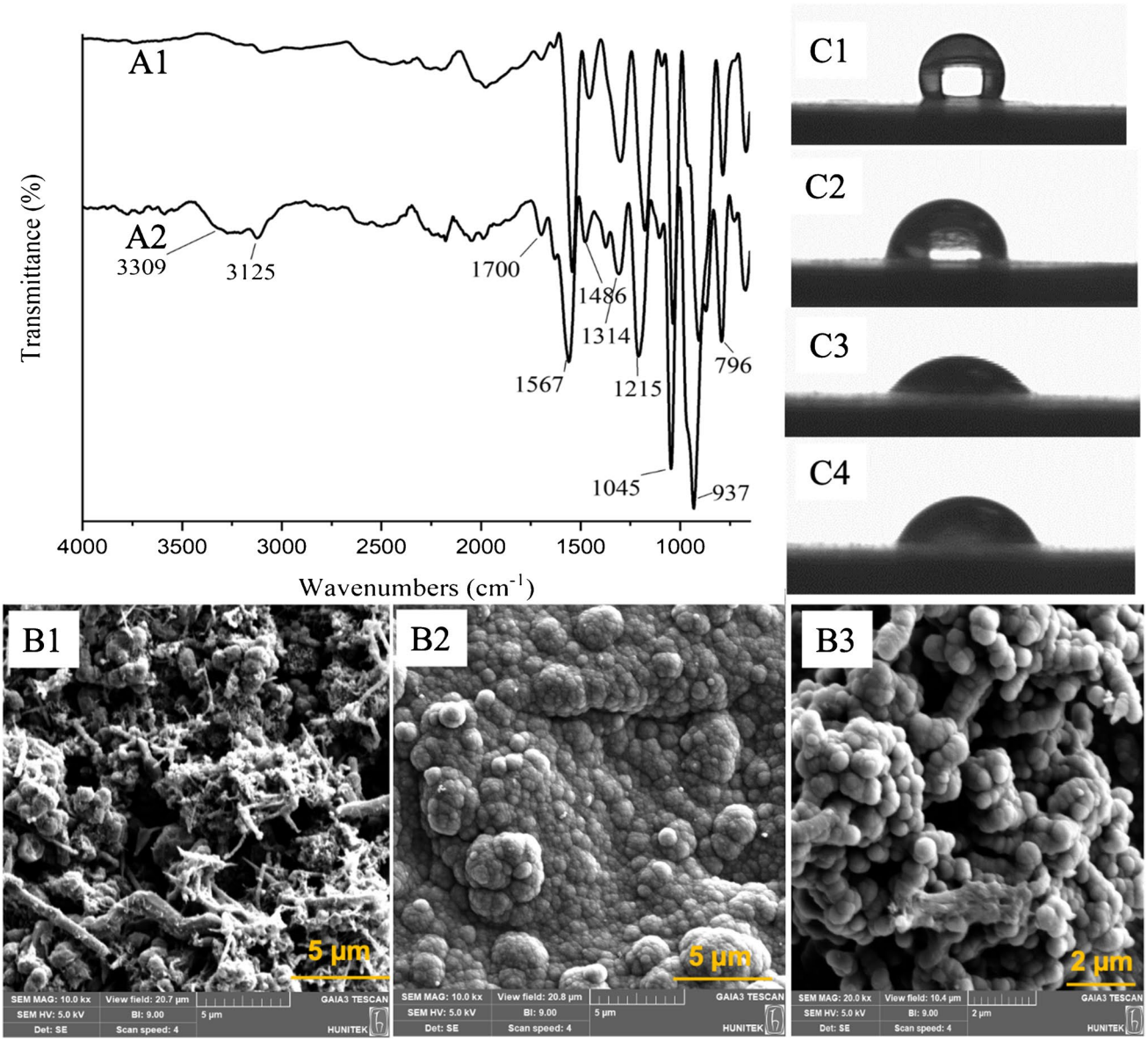


**Fig. 2** **A** ATR-FTIR spectra of Thy@CNFs/MIP/GCE (**A1**) and Thy@CNFs/NIP/GCE (**A2**), **B** SEM images of Thy@CNFs/GCE (**B1**), Thy@CNFs/NIP/GCE (**B2**), and Thy@CNFs/MIP/GCE (**B3**), and (**C**) contact angle images of bare GCE (**C1**), Thy@CNFs/GCE (**C2**), Thy@CNFs/MIP/GCE (**C3**), and Thy@CNFs/NIP/GCE (**C4**)

amino-groups on the polymeric film was also the reason for decreasing contact angle values.

## Electrochemical characterization of modified electrodes

The electrochemical characterization of GCE at different stages of modification and molecular imprinting steps was characterized by CV and EIS measurements. A solution containing 5 mM potassium ferricyanide in 0.1 mol $L^{-1}$ KCl was employed, with the oxidation potential set based on the values determined by cyclic voltammetry (CV) at each experimental stage. The various steps were evaluated based on their charge transfer resistance (Rct), derived from the Nyquist plots fitted using the Randles equivalent circuit. This circuit includes the solution resistance (Rs), a constant phase element (CPE), the charge transfer resistance (Rct), and a Warburg diffusion element (W).

Figure 3 shows (A) CVs and (B) Nyquist plots for (a) GCE, (b) Thy@CNFs/GCE, (c) Thy@CNFs/MIP/GCE (polymerization), (d) Thy@CNFs/MIP/GCE (after template removal), and (e) Thy@CNFs/MIP/GCE (rebinding). In the cyclic voltammetry (CV) analyses, the modification of the bare GCE with Thy@CNFs (b) led to a significant

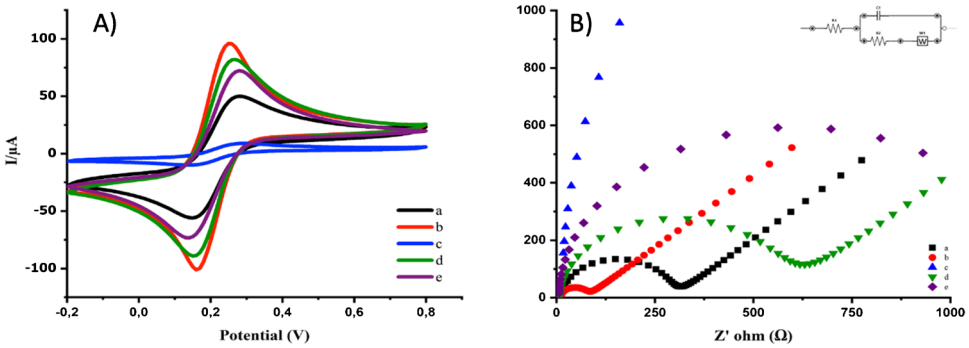


**Fig. 3** **A** CV and **B** EIS measurements of electrochemical sensors. (a) GCE, (b) Thy@CNFs/GCE, (c) Thy@CNFs/MIP/GCE (polymerization), (d) Thy@CNFs/MIP/GCE (after template removal), and (e) Thy@CNFs/MIP/GCE (rebinding) (measurements were conducted in 5.0 mM $[Fe(CN)6]^{3-/4-}$ under the following conditions: −0.2 to +0.8 V scan range, 1.587 mV $s.^{-1}$ scan rate, 8 mV step, 50 mV modulation amplitude, 0.05 s modulation time, and 0.5 s interval)

increase in peak current to 95.89 µA, compared to 45.15 µA for the bare GCE (a). This enhancement can be attributed to the increased electroactive surface area and improved conductivity provided by the conductive nanofiber composite, which facilitates more efficient electron transfer. Following the electrodeposition of the MIP layer onto the Thy@CNFs-modified surface (c), the peak current markedly decreased to 7.62 µA, indicating that the polymer film partially obstructed the electrode surface and limited redox probe access. Upon removal of the template molecules (d), specific recognition sites were exposed within the polymer matrix, improving accessibility for the redox probe and resulting in a peak current increase to 79.56 µA. During the rebinding step (e), the target analyte reoccupied the recognition cavities, partially blocking electron transfer pathways and causing a further decrease in peak current to 64.28 µA. The electrochemical impedance spectra (EIS) presented in Fig. 3B demonstrate the stepwise surface modification of the electrode. The bare GCE exhibits a distinct semicircular region in the Nyquist plot, corresponding to a relatively high charge transfer resistance (Rct) of 277.8 Ω (a), which reflects moderate electron transfer kinetics. After modification with CNF@Thy (b), the Rct value significantly decreases to 65.5 Ω, indicating that the conductive and porous nanofiber composite enhances the electron transfer of the $[Fe(CN)_6]^{3-/4-}$ redox probe. Upon electrodeposition of the imprinted polymer film onto the modified electrode surface (c), the Rct increases to 6249 Ω, confirming the formation of a compact and insulating layer that restricts electron transfer and impedes the diffusion of the redox probe. Following the removal of template molecules from the polymer matrix (d), the Rct value decreases to 554.9 Ω due to the formation of specific recognition cavities within the polymer network, which facilitate probe access. However, the resistance remains higher than that of the bare electrode, likely due to the relatively low molecular weight of the target molecule compared to the thickness of the polymer layer. Finally, after incubation with the HYP solution (e), the Rct increases to 1187 Ω, which may be attributed to the rebinding of template molecules into the imprinted cavities, thereby partially hindering the interaction of the redox probe with the electrode surface. Despite the enhanced current responses observed in cyclic voltammetry (CV), likely due to localized electroactive regions, electrochemical impedance spectroscopy (EIS) reveals hindered overall charge transfer. This difference may result from a non-uniform composite architecture, inadequate dispersion, and alignment of conductive nanofibers, or elevated capacitive effects from the polymer matrix. For instance, the impedance of glassy carbon electrodes modified with a polypyrrole composite was analyzed, showing that the impedance characteristics are influenced by the internal structure of the material and the level of oxidation [32]. Additionally, the impedance of polypyrrole/carbon nanotube composites was found to decrease, which suggests that the impedance behavior can vary depending on the specific composite structure and conditions [33]. One more example, a composite electrode of polypyrrole- and carbon-based materials demonstrated a specific capacitance that was 2.3–2.5 times higher than that of the modified electrode alone, and the charging resistance was dramatically reduced [34]. This suggests that the composite structure can lead to both increased current and modified impedance characteristics. On the other hand, the structural features of the composite materials, such as the distribution, aligment, and interaction between the conjugated polymers and carbon nanofibers, play a crucial role in their electrochemical properties. The intermolecular interactions between polymers in carbon nanofibers influence their thermal and electrochemical properties, leading to improved performance [32]. Additionally, excessive coating thickness or a disrupted percolation network can introduce mass transport limitations and interfacial resistance, further contributing to increased impedance.

## Optimization of the conditions

Optimization studies in MIP electrochemical sensors have been examined to ensure the analytical performance of the sensor developed for HYP detection. The differential pulse voltammograms of developed sensors were utilized to assess the response of each electrode by using redox probe, $[Fe(CN)_6]^{3-/4-}$. Parameters such as Thy@CNFs dropping volume, rebinding time, and number of cycles for electropolymerization/removal were optimized to obtain stable and efficient MIP-based electrochemical sensors. The effect of Thy@CNFs amount on the electrochemical sensor was studied for preparing the Thy@CNFs/GCE electrodes. For this purpose, eight modified GCEs were designed between 0.5 and 5.0 µL of Thy@CNFs dispersion. Figure 4A shows that the peak current increased with Thy@CNFs amount due to the high conductivity and unique structure of CNFs. After a certain point, there was a decrease in the peak current, which may occur due to the aggregation of Thy@CNFs and the disruption of the homogeneous distribution of CNFs on the electrode surface. Therefore, the optimum value was determined as 1.0 µL and kept constant for further studies to increase conductivity and facilitate polymerization.

Electropolymerization is a critical step for creating an effective and stable polymeric coating in a proper film thickness. The electropolymerization of Py-co-PyCOOH in the presence of a template has been examined by CV cycles. The effect of cycle number for polymerization on the performance of the Thy@CNFs/GCE/MIP was investigated in the range of 3–20 cycles (Fig. 4B). The peak currents increased with increase of cycle number until 10 cycles and then remained stable.

In this respect, 10 cycles were assigned as the most stable and time-efficient parameter for electropolymerization. On the other hand, the increases in current peaks during successive cycles indicate that electropolymerization has successfully occurred. It is known that the removal agent significantly affects the effective removal of HYP from the polymeric network. HYP molecule was extracted from the polymeric film with varying numbers of cycles (3, 5, 8, 10, and 15) by using 1.0 M NaCl (pH 8.0) to identify the most effective removal cycles. The peak current increased in the subsequent cycles until the tenth cycle and then remained stable, which showed that 10 cycles were sufficient to remove HYP from the polymeric network to expose the complementary cavities (Fig. 4C), successfully.

Finally, it was also evaluated the rebinding time of HYP to the MIP in the varying time interval from 5 to 30 min to determine the most appropriate rebinding duration. A continuous increase in the current response was measured up to 20 min of incubation, and then the signal remained constant (Fig. 4D). In this respect, the rebinding steps were performed for 20 min during all studies. As a summary, the optimum values for affecting factors including amount of Thy@CNFs, the numbers of CV cycles for both of electropolymerization and template removal, and rebinding time were determined as 1.0 µL, 10 cycles, and 20 min, respectively.

## Quantitative analysis of HYP on Thy@CNFs/GCE/MIP

Under the optimum conditions, the quantitative analysis of HYP with different concentrations on Thy@CNFs/GCE/MIP was performed by DPV. As seen in Fig. 5A, the peak current exhibited a decrease with the increase in HYP concentration. As the HYP bound to the recognition sites in the MIP structure, it effectively blocked these cavities, inhibiting the diffusion of $[Fe(CN)_6]^{3-/4-}$ to surface.

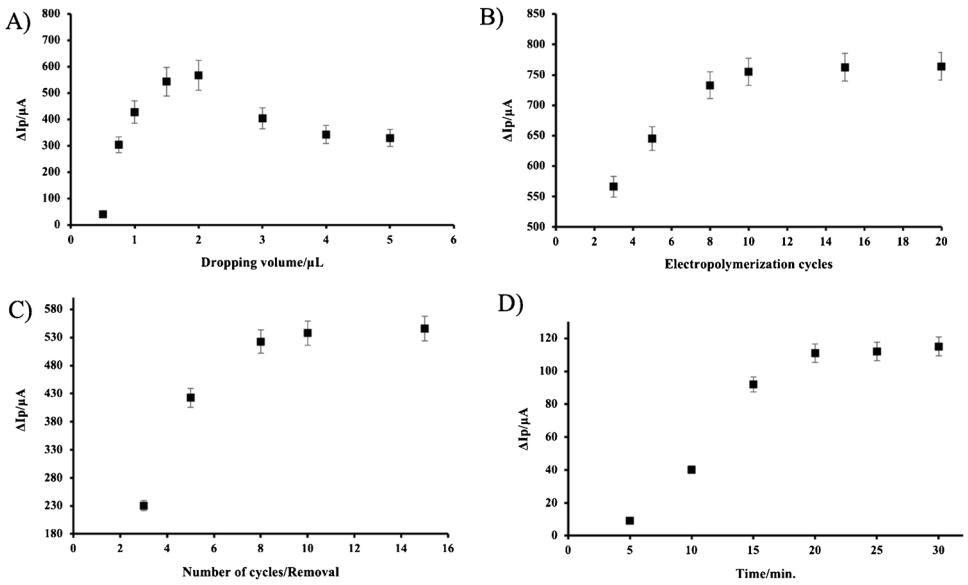


**Fig. 4** The plots of optimizing parameter values versus **A** dropping volume, **B** electropolymerization cycle, **C** template removal cycle, and **D** rebinding time (measurements were conducted in 5.0 mM $[Fe(CN)6]^{3-/4-}$ under the following conditions: −0.2 to +0.8 V scan range, 1.587 mV $s.^{-1}$ scan rate, 8 mV step, 50 mV modulation amplitude, 0.05 s modulation time, and 0.5 s interval)

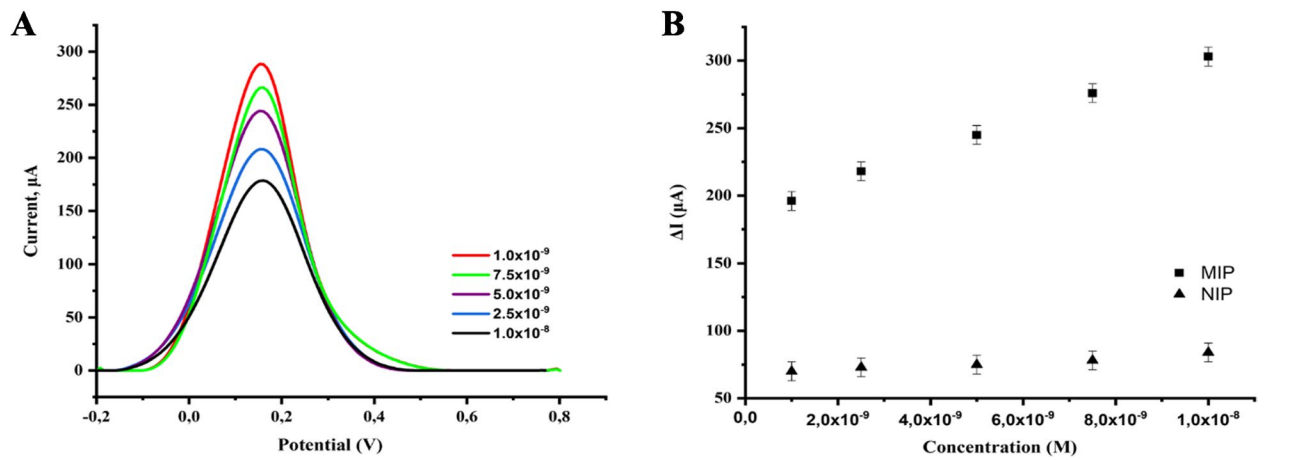


**Fig. 5** **A** DPV voltammograms of the Thy@CNFs/GCE/MIP with HYP concentrations and **B** calibration curves obtained for MIP and NIP sensors (measurements were conducted in 5.0 mM $[Fe(CN)6]^{3-/4-}$ under the following conditions: −0.2 to +0.8 V scan range, 1.587 mV $s.^{-1}$ scan rate, 8 mV step, 50 mV modulation amplitude, 0.05 s modulation time, and 0.5 s interval)

This inhibition of electron transport results in a decrease in current (Fig. 5A) as expected. The binding specificity arises as the imprinted cavities are tailored to the shape and functional groups of HYP. Therefore, more HYP molecules occupy the available spaces and the accessibility for the redox probe decreases further, causing the sensor's current to decrease proportionally. This principle underlies the use of MIPs in sensing applications to detect specific analytes with high selectivity. In healthy individuals, the normal concentration of hypoxanthine (HYP) in erythrocytes is 9.3 nm and it ranges from 0.5 to 11 µmol/L in blood [35, 36].

Therefore, we focused on the concentration range of 1.0 to 10.0 nmol/L. As shown in Fig. 5B, a linear relationship was observed between the current response (ΔI, µA) and the concentration of HYP (CHYP, M). The Thy@CNFs/GCE/MIP presented a good linear relationship with the HYP concentration ranging from $1.0\times10^{-9}$ to $1.0\times10^{-8}$ M. The linear regression equation was shown as follows: $\Delta I\ (\mu A) = 1.0\times10^{10} C\ (M) + 183.3$ with a high correlation coefficient ($r = 0.9948$). A summary of the regression parameters is presented in Table S1. Using the regression data, LOD and LOQ were calculated as $1.71\times10^{-10}$ M and $5.69\times10^{-10}$ M (S/N = 3), respectively. The limit of detection (LOD) and limit of quantification (LOQ) were determined based on the guidelines of the International Union of Pure and Applied Chemistry (IUPAC), using Eqs. 1 and 2. LOD = 3.3 × standard deviation/slope (Eq. 1), LOQ = 10 × standard deviation/slope (Eq. 2). Both parameters were obtained from three replicate measurements. These values demonstrate the high sensitivity of the sensor, enabling accurate detection and measurement of HYP at trace levels, making it suitable for applications requiring highly sensitive analytical techniques. Unlike the MIP-based sensor, the NIP-based sensor did not show any significant response, suggesting a non-linear response over the HYP concentration, possibly owing to the absence of specific recognition sites.

## Application of Thy@CNFs/GCE/MIP for real samples

To assess the practical application of the MIP sensor in real sample analysis, Thy@CNFs/GCE/MIP was used to determine HYP in commercial serum and urine sample. Recovery studies for commercial serum and urine sample were conducted using three replicate measurements at the midpoint concentration of the calibration curve. The average recovery values were determined to be 99.55% for serum and 100.17% for urine, with corresponding RSD values of 1.04% and 1.18%, respectively, indicating acceptable accuracy and precision of the method. The present method showed good recovery for the simultaneous determination of HYP in commercial serum and urine sample. The results indicate that the presented method could be efficiently used to determine the

**Table 2** Recovery study outcomes for biological matrices: commercial serum and urine sample

| | Electrochemical sensor | | HPLC–DAD | |
|---|---|---|---|---|
| | Commercial serum sample | Urine sample | Commercial serum sample | Urine sample |
| **Spiked (M)** | $7.50\times10^{-9}$ | $7.50\times10^{-9}$ | $7.35\times10^{-6}$ | $7.35\times10^{-6}$ |
| **Found (M)** | $7.46\times10^{-9}$ | $7.51\times10^{-9}$ | $7.47\times10^{-6}$ | $7.41\times10^{-6}$ |
| **Recovery (%)** | 99.55 | 100.17 | 101.63 | 100.82 |
| **RSD%** | 1.04 | 1.18 | 1.56 | 1.42 |

Each value is the mean of three experiments

RSD% = (standard deviation)/(mean recovery)*100

HYP in real samples. The results obtained from the recovery studies are summarized in Table 2. In addition, the recovery results obtained using the fabricated sensor were compared with those of the standard **HPLC–DAD** method for HYP determination, as presented in Table 2. The results demonstrate that the developed sensor can serve as a reliable alternative for the quantification of HYP in serum and urine samples, offering high sensitivity and excellent recovery values. The chromatograms of real samples are provided in detail in Fig. S6 of the Supplementary File.

## Selectivity studies

Selectivity studies were also obtained using xanthine (XAN) and uracil (UA), which have a stereo-chemical similarity regarding shape, size, and functional group affinity with HYP. The selectivity of the sensor was evaluated by comparing its response to the target molecule and to structurally similar analogs. The ΔI value was calculated as the difference between the current measured after template removal and after rebinding of either the template molecule or the analogs. The selectivity coefficients of HYP over XAN and UA were determined to be 2.74 and 3.44, respectively (Table 3). The results pointed out that Thy@CNFs/GCE/MIP sensor selectively recognized HYP compared to other products of purine metabolism in humans, XAN and UA.

**Table 3** The selectivity coefficients ($k$) and relative selectivity coefficient ($k\prime$) values for Thy@CNFs/GCE/MIP and Thy@CNFs/GCE/NIP

| | MIP/GCE | | NIP/GCE | | |
|---|---|---|---|---|---|
| Molecules | **ΔI/μA** | $\mathbf{k_{(MIP)}}$ | **ΔI/μA** | $\mathbf{k_{(NIP)}}$ | $\mathbf{k'_{(MIP/NIP)}}$ |
| HYP | 288 | – | 107 | – | – |
| XAN | 117 | 2.46 | 119 | 0.90 | 2.74 |
| UA | 101 | 2.85 | 129 | 0.83 | 3.44 |

The selectivity coefficient quantifies how well the sensor distinguishes the target assay (template) from other similar molecules and is defined as $k$, ($k = \Delta I_{template}/\Delta I_{othermolecule}$ while the relative selectivity coefficient $k\prime$, ($k\prime = k_{MIP}/k_{NIP}$) indicates the magnitude of selectivity achieved by MIP compared to NIP, with a value greater than one indicating that MIP is more selective towards the analyte. The results prove that the prepared sensor shows higher selectivity for the template molecule compared to similar compounds.

## Comparison of selected sensors

The comparative analysis presented in Table 4 highlights the analytical performance of the Thy@CNFs/MIP/GCE sensor developed in this study. While previously reported sensors demonstrate detection limits ranging from micromolar to nanomolar levels, the proposed sensor achieves an ultralow limit of detection (LOD) of $0.171 \times 10^{-9}$ M. This enhanced performance can be attributed to the synergistic effect of thymine-functionalized carbon nanofibers (Thy@CNFs), which improve film morphology and conductivity, and the molecular imprinting technique that provides high selectivity through the creation of specific recognition sites for HYP.

The selectivity was also further supported by favorable recovery values of 99.55% (serum) and 100.17% (urine), and low RSDs (≤1.18%), confirming both the accuracy and precision of the method in real sample applications. Furthermore, the sensor demonstrated successful applicability in complex matrices, including serum and artificial urine, yielding high recovery rates. Overall, the results shows that integrating functionalized carbon nanofibers with molecularly imprinted polymer (MIP) technology holds significant promise for the development of next-generation electrochemical sensors, with practical applicability in biomedical monitoring.

**Table 4** Comparison of analytical performance of various hypoxanthine sensors with the proposed Thy@CNFs/MIP/GCE sensor

| Sensor material/method | Linear range | LOD | Real sample | Recovery (%) | Reference |
|---|---|---|---|---|---|
| GC/HDA/ERGO/GCE | 5–300 μM | 0.32 | Serum, urine | 99.0–99.4<br>98.3–100.4 | [37] |
| Poly(bromocresol purple)/GCE | 0.20–80 μM | 0.12 μM | Serum | 97.9–99.3 | [38] |
| Poly (ATD)/GCE | 0.37–73.5 μM | 0.074 μM | Urine | 94–98 | [39] |
| CMC-Pal-NG/GCE | 0.6–55 μM | 1.3 μM | Serum | 100.5 | [40] |
| Poly(l-arginine)/RGO/GCE | 0.2–20 μM | 0.1 μM | Urine | 94–102 | [41] |
| B-$CeO_2$NCs/GCPE | 0.4–60 μM | 6.17 nM | Serum | 96.62–101.26 | [42] |
| Poly (PCV)/MWCNT/GCE | 0.5–90 μM | 0.2 μM | Serum | 97.5–98.9 | [43] |
| rGO/GCE | 0.43–7.39 μM | 0.141 μM | Plasma | 97.8–108.5 | [44] |
| p-Gly/rGO/GCE | 1–100 μM | 0.2 μM | Serum | 95.5–103.0 | [45] |
| Thy@CNFs/MIP/GCE | 1–10 nM | 0.171 nM | Serum, urine | 99.5–100.17 | In this study |

## Conclusion

In this work, we showed that the composite film for the determination of HYP combines the advantages of selectivity of MIP and conductivity of poly(Py-co-PyCOOH). The poly(Py-co-PyCOOH) composite film was successfully fabricated with excellent recognition capabilities and formed on the surfaces of Thy@CNFs as a new highly sensitive and selective electrochemical for HYP detection. The experimental methods of CV, EIS, and DPV with developed sensors provide an opportunity for the qualitative and quantitative characterization and determination of HYP. Thymine promoted MIP orientation and the formation of uniform imprinting areas, benefiting HYP's recognition and rebinding. Furthermore, Thy@CNFs enhanced conductivity and sensitivity for electrochemical sensing. Thus, Thy@CNFs/MIP/GCE has excellent sensing performance for determining MP, with an LOD of $1.71 \times 10^{-10}$ M (S/N = 3) and linear concentration ranges of $1.0 \times 10^{-9}$–$1.0 \times 10^{-8}$ M. Thymine-modified CNFs contributed to improved film morphology, enhanced imprinting efficiency, and facilitated rebinding by providing a specific interaction sites for hypoxanthine and conductive surface. These provided more accessible and well-defined recognition sites, thereby enhancing the sensor's rebinding dynamics and overall sensitivity.

This study demonstrates the utility of advanced electrochemical techniques for analyzing clinically significant biomolecules, showcasing a sensitive, accurate, and adaptable method for real applications.

**Supplementary Information** The online version contains supplementary material available at https://doi.org/10.1007/s00604-025-07502-5.

**Author contributions** Canan Armutcu: Supervision, Conceptualization, Writing–review & editing. Sena Piskin: Investigation, Conceptualization, Writing–original draft. Erdoğan Özgür: Supervision, Conceptualization, Writing–review & editing. Mustafa Karakaya: Supervision, Conceptualization, Writing–review & editing. M. Emin Çorman: Supervision, Conceptualization, Writing–review & editing. Lokman Uzun: Supervision, Conceptualization, Writing–review & editing.

**Data availability** No datasets were generated or analysed during the current study.

## Declarations

**Competing interests** The authors declare no competing interests.

## References


1. Beloborodova NV, Olenin AY, Pautova AK (2018) Metabolomic findings in sepsis as a damage of host-microbial metabolism integration. J Crit Care 43:246–255
2. Kalogeris T, Baines CP, Krenz M, Korthuis RJ (2017) Ischemia/reperfusion. Compr Physiol 7:113–170
3. Mileti LN, Baleja JD (2025) The role of purine metabolism and uric acid in postnatal neurologic development. Molecules 30:839
4. Dervisevic M, Dervisevic E, Şenel M (2019) Recent progress in nanomaterial-based electrochemical and optical sensors for hypoxanthine and xanthine. A review, Microchim Acta 186:749
5. Çorman ME, Cetinkaya A, Armutcu C, Atici EB, Uzun L, Ozkan SA (2022) A sensitive and selective electrochemical sensor based on molecularly imprinted polymer for the assay of teriflunomide. Talanta 249:123689
6. Çorman ME, Cetinkaya A, Armutcu C, Uzun L, Ozkan SA (2023) Designing of ZnO nanoparticles oriented interface imprinted electrochemical sensor for fluoxetine detection. Bioelectrochemistry 152:108411
7. Karadurmus L, Corman ME, Uzun L, Ozkan SA (2022) Enantioselective recognition of esomeprazole with a molecularly imprinted sol–gel-based electrochemical sensor. Microchim Acta 189:225
8. Hinman SS, Cheng Q (2016) Bioinspired assemblies and plasmonic interfaces for electrochemical biosensing. J Electroanal Chem 781:136–146
9. Cetinkaya A, Unal MA, Nazır H, Çorman ME, Uzun L, Ozkan SA (2024) A comparative study of electropolymerization and photopolymerization for the determination of molnupiravir and their application in an electrochemical sensor via computationally designed molecularly imprinted polymers. Microchim Acta 191:270
10. Pérez JAC, Sosa-Hernández JE, Hussain SM, Bilal M, Parra-Saldivar R, Iqbal HM (2019) Bioinspired biomaterials and enzyme-based biosensors for point-of-care applications with reference to cancer and bio-imaging. Biocatal Agric Biote 17:168–176
11. Wang L, Li W, Wu B, Li Z, Wang S, Liu Y, Pan D, Wu M (2016) Facile synthesis of fluorescent graphene quantum dots from coffee grounds for bioimaging and sensing. Chem Eng J 300:75–82
12. Chen F, Lv C, Xing Y, Luo L, Wang J, Cheng Y, Xie X (2023) Electrospinning carbon fibers based molecularly imprinted polymer self-supporting electrochemical sensor for sensitive detection of glycoprotein. Sens Actuators, B Chem 396:134552
13. Gomes-Filho S, Dias A, Silva M, Silva B, Dutra R (2013) A carbon nanotube-based electrochemical immunosensor for cardiac troponin T. Microchem J 109:10–15
14. Jeon SS, Kim C, Ko J, Im SS (2011) Spherical polypyrrole nanoparticles as a highly efficient counter electrode for dye-sensitized solar cells. J Mater Chem 21:8146–8151
15. Maziz A, Özgür E, Bergaud C, Uzun L (2021) Progress in conducting polymers for biointerfacing and biorecognition applications. Sensor Actuator Rep 3:100035
16. Koklu A, Ohayon D, Wustoni S, Druet V, Saleh A, Inal S (2021) Organic bioelectronic devices for metabolite sensing. Chem Rev 122:4581–4635
17. Goyal M, Singh K, Bhatnagar N (2024) Conductive polymers: a multipurpose material for protecting coating. Prog Org Coat 187:108083
18. Wysocka-Żołopa M, Brzózka A, Zambrzycka-Szelewa E, Klekotka U, Kalska-Szostko B, Winkler K (2023) Structure and electrochemical properties of magnetite and polypyrrole nanocomposites formed by pyrrole oxidation with magnetite nanoparticles. J Solid State Electr 27:1919–1934
19. Roy CJ, Leprince L, De Boulard A, Landoulsi J, Callegari V, Jonas AM, Demoustier-Champagne S (2011) Electrosynthesis of pyrrole 3-carboxylic acid copolymer films and nanotubes with tunable degree of functionalization for biomedical applications. Electrochim Acta 56:3641–3648
20. Rozi N, Hanifah SA, Zaid MHM, Abd Karim NH, Ikeda M (2021) Feasible study on poly (pyrrole-co-pyrrole-3-carboxylic

acid)-modified electrode for detection of 17β-Estradiol. Chem Pap 75:3493–3503
21. Becke AD (1992) Density-functional thermochemistry.1. The effect of the exchange-only gradient correction, J Chem Phys 96:2155–2160. https://doi.org/10.1063/1.462066
22. Hohenberg P, Kohn W (1964) Inhomogeneous electron gas. Phys Rev 136:B864
23. Simon S, Duran M, Dannenberg JJ (1996) How does basis set superposition error change the potential surfaces for hydrogen bonded dimers? J Chem Phys 105:11024–11031. https://doi.org/10.1063/1.472902
24. Glendening E, Reed A, Carpenter J, Weinhold F (1990) NBO 3.0 program manual, Theoretical Chemistry Institute, University of Wisconsin, Madison, WI,
25. Dennington R, Keith T, Millam J (2009) GaussView, version 5
26. BIOVIA DS (2021) Discovery Studio Visualizer 4.5, San diego: Dassault systèmes
27. Chutipongtanate S, Thongboonkerd V (2010) Systematic comparisons of artificial urine formulas for in vitro cellular study. Anal Biochem 402:110–112
28. Karakaya M, Yildiz M (2015) A study on optimum transition state and tautomeric structures of a bis-heterocyclic monoazo dye. Indian J Phys 89:107–114
29. Almutairi MS, Xavier S, Sathish M, Ghabbour HA, Sebastian S, Periandy S, Al-Wabli RI, Attia MI (2017) Spectroscopic (FT-IR, FT-Raman, UV, H and C NMR) profiling and computational studies on methyl 5-methoxy-1H-indole-2-carboxylate: a potential precursor to biologically active molecules. J Mol Struct 1133:199–210
30. Özdemir N, Eren B, Dinçer M, Bekdemir Y (2010) Experimental and ab initio computational studies on 4-(1H-benzo[d]imidazol-2-yl)-N. N-dimethylaniline, Mol Phys 108:13–24
31. Politzer P, Murray JS (2002) The fundamental nature and role of the electrostatic potential in atoms and molecules. Theor Chem Acc 108:134–142
32. Torres W, Carabali MA (2021) Impedance spectra analysis of glassy carbon/(polypyrrole+ polystyrene sulfonate) electrodes by using a modified randles equivalent circuit with a constant phase element. ECS Trans 100:3
33. Ben-Valid S, Botka B, Kamarás K, Zeng A, Yitzchaik S (2010) Spectroscopic and electrochemical study of hybrids containing conductive polymers and carbon nanotubes. Carbon 48:2773–2781
34. Cai Y, Wang Y, Han X, Zhang L, Xu S, Wang J (2016) Optimization on electrode assemblies based on ion-doped polypyrrole/carbon nanotube composite in capacitive deionization process. J Electroanal Chem 768:72–80
35. Cardinale AN, Di Lorenzo A, Bellino M, Strisciullo G, Mussi V, Sablone S (2025) Thanatochemistry and the role of hypoxanthine in the post-mortem interval estimation: a systematic literature review, Int J Leg Med 1–38
36. Casali E, Berni P, Spisni A, Baricchi R, Pertinhez TA (2015) Hypoxanthine: a new paradigm to interpret the origin of transfusion toxicity. Blood Transfus 14:555
37. Raj MA, John SA (2013) Simultaneous determination of uric acid, xanthine, hypoxanthine and caffeine in human blood serum and urine samples using electrochemically reduced graphene oxide modified electrode. Anal Chim Acta 771:14–20
38. Wang Y, Tong L-l (2010) Electrochemical sensor for simultaneous determination of uric acid, xanthine and hypoxanthine based on poly (bromocresol purple) modified glassy carbon electrode. Sens Actuators, B Chem 150:43–49
39. Cai X, Kalcher K, Neuhold C (1994) Simultaneous determination of uric acid, xanthine and hypoxanthine with an electrochemically pretreated carbon paste electrode. Fresenius J Anal Chem 348:660–665
40. Wen Y, Chang J, Xu L, Liao X, Bai L, Lan Y, Li M (2017) Simultaneous analysis of uric acid, xanthine and hypoxanthine using voltammetric sensor based on nanocomposite of palygorskite and nitrogen doped graphene. J Electroanal Chem 805:159–170
41. Zhang F, Wang Z, Zhang Y, Zheng Z, Wang C, Du Y, Ye W (2012) Simultaneous electrochemical determination of uric acid, xanthine and hypoxanthine based on poly (l-arginine)/graphene composite film modified electrode. Talanta 93:320–325
42. Ibrahim H, Temerk Y (2016) A novel electrochemical sensor based on B doped CeO2 nanocubes modified glassy carbon microspheres paste electrode for individual and simultaneous determination of xanthine and hypoxanthine. Sens Actuators, B Chem 232:125–137
43. Wang Y (2011) Simultaneous determination of uric acid, xanthine and hypoxanthine at poly (pyrocatechol violet)/functionalized multi-walled carbon nanotubes composite film modified electrode. Colloids Surf, B 88:614–621
44. Kablan SE, Yılmaz A, Kervan Ü, Özaltın N, Nemutlu E (2023) Electrochemically based targeted metabolomics for uric acid, xanthine, and hypoxanthine in plasma samples for early diagnosis of acute renal failure after cardiopulmonary bypass using rGO-GCE. Talanta 253:124005
45. Wang T, Zhang L, Zhang C, Deng D, Wang D, Luo L (2023) Simultaneous determination of xanthine and hypoxanthine using polyglycine/rGO-modified glassy carbon electrode. Molecules 28:1458